PAPER

Check for updates

Cellular fate and performance of group IV metal organic framework radioenhancers†

Anna Lena Neuer, [ID] [a,b] Alexander Jessernig, [a,b] Lukas R. H. Gerken, [ID] [a,b] Alexander Gogos, [ID] [a,b] Fabian H. L. Starsich, [ID] [a,b] Alexandre H. C. Anthis [a,b] and Inge K. Herrmann [ID] *[a,b]

Nano-sized metal organic frameworks (nanoMOFs) have gained increasing importance in biomedicine due to their tunable properties. In addition to their use as carriers in drug delivery, nanoMOFs containing hafnium have been successfully employed as radio-enhancers augmenting damage caused by X-ray irradiation in tumor tissue. While results are encouraging, there is little mechanistic understanding available, and the biological fate of these radio-enhancer nanoparticles remains largely unexplored. Here, we synthesized a selection of group IV metal-based (Hf, Ti, Ti/Zr) nanoMOFs and investigated their cell compatibility and radio-enhancement performance in direct comparison to the corresponding metal oxides. We report surprising radio-enhancement performance of Ti-containing nanoMOFs reaching dose modifying ratios of 3.84 in human sarcoma cells and no relevant dose modification in healthy human fibroblasts. These Ti-based nanoMOFs even outperformed previously reported Hf-based nanoMOFs as well as equimolar group IV metal oxides in direct benchmarking experiments. While group IV nanoMOFs were well-tolerated by cells in the absence of irradiation, the nanoMOFs partially dissolved in lysosomal buffer conditions showing distinctly different chemical stability compared to widely researched group IV oxides (TiO_2, ZrO_2, and HfO_2). Taken together, this study illustrates the promising potential of Ti-based nanoMOFs for radio-enhancement and provides insight into the intracellular fate and stability of group IV nanoMOFs.

Introduction

Radiotherapy is a key treatment modality in cancer therapy. Despite its wide applicability, X-ray radiation suffers from poor tissue specificity. The radiation penetration depth and the total dose applied to the tumor are limited by the radiation tolerance of the healthy tissue surrounding the tumor.[1–3] In order to overcome these limitations and at the same time maximize the dose deposited in the diseased tissue, different strategies have been exploited. These include sophisticated treatment planning, beam modulation, or the use of complex beam geometries. Additionally, the radio-sensitizing effects of chemotherapeutic agents have been exploited with the aim of increasing the radiation susceptibility of diseased cells.[4] However, the advancement of the aforementioned approaches have plateaued and new strategies are sought after in order to further augment the effectiveness of radiotherapy. Radio-enhancing metal or metal oxide nanoparticles can serve as promising alternatives to existing approaches.[5] Inorganic nanoparticles selectively enhance the X-ray absorption cross-section leading to locally enhanced tissue damage in their vicinity compared to particle-free volumes. A wide variety of metal and metal oxide nanoparticles have been investigated, including gold,[6,7] platinum,[8,9] and others (see Kuncic *et al.*[10] for a comprehensive review). If these nanoparticles accumulate inside a tumor, they efficiently absorb the energy of the incoming photon beam. The absorbed energy can then lead to the ejection of secondary particles, such as electrons, and depending on the metal oxide and the incident X-ray energy, these secondary electrons can travel from only a couple of μm to a few hundreds of μm.[10] On their way through tissue, they produce significant amounts of reactive oxygen species (ROS) through ionization events, which can ultimately lead to cell death.[11] As the amount of ROS produced is proportional to the accessible surface area, significant effort has been invested into reducing the nanoparticle sizes to maximize the specific

[a]Laboratory for Particles-Biology Interactions, Department of Materials Meet Life, Swiss Federal Laboratories for Materials Science and Technology (Empa), Lerchenfeldstrasse 5, 9014 St. Gallen, Switzerland. E-mail: inge.herrmann@empa.ch, ingeh@ethz.ch; Tel: +41 (0)58 765 7153
[b]Nanoparticle Systems Engineering Laboratory, Institute of Process Engineering, Department of Mechanical and Process Engineering, ETH Zurich, Sonneggstrasse 3, 8092 Zurich, Switzerland
†Electronic supplementary information (ESI) available. See DOI: https://doi.org/10.1039/d2bm00973k

surface area.[12] However studies have found that smaller particles can in some cases be more cytotoxic compared to their larger counterparts,[13] thus constraining the therapeutic window. Alternatively, nano-sized metal organic frameworks (nanoMOFs) offer a large specific surface area and high compositional modularity, and thus offer a route to unify high specific surface area with biocompatibility. MOFs are three-dimensional coordination polymers composed of secondary building units (SBUs) assembled into a porous lattice structure. The SBUs are generated through the coordinative interaction between metal ion clusters and polydentate organic linker molecules.[14,15] This so-called reticular synthesis allows the use of a considerable variety of metals and linkers giving rise to fascinating design possibilities.[16,17] Combined with recent advances in nanoparticle synthesis, MOFs have shown great promise in a number of applications ranging from catalysis to biomedicine.[18–20] First reports of nanoMOFs as radioenhancers were published in 2018 when the Lin group used hafnium-based SBUs to synthesize high-Z nanoMOFs. By comparing two Hf-MOFs that differ in their SBU, they not only showed that the SBU choice influences the X-ray absorption efficiency but also confirmed that a larger surface area leads to increased ROS production.[21] Several of their studies have shown that Hf-based nanoMOFs exhibit radio-enhancement efficiencies surpassing even those of HfO_2 nanoparticles, which have most recently been approved as NBTXR3 for clinical use in soft tissue sarcoma and other tumor treatments.[22] While various linkers have been probed in nanoMOFs for radiotherapy purposes, there is surprisingly little variation in the choice of the metal centers and studies have focused primarily on hafnium. In addition to poorly understood radio-enhancement mechanisms of metal-based radio-enhancers, the biological fate of nanoMOFs is still largely unexplored. It is well-known that group IV metals, including hafnium, are prone to oxidation in biological environments.[23] Compared to metal oxides, the administration of nanoMOFs involves the introduction of a potentially more labile form of group IV non-essential metals into biological systems, with yet poorly understood consequences.
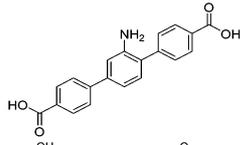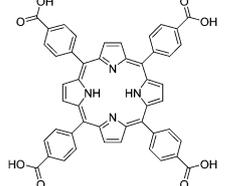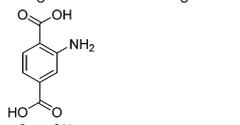
In this work, we synthesized Hf-DBA, Hf-TCPP, Ti-MIL-125, and Ti/Zr-PCN-415 group IV nanoMOFs as radioenhancer candidate materials. Following physicochemical characterization, buffer stability and cytocompatibility assessment, we investigated their radioenhancement activity under X-ray irradiation based on ROS detection (in cell free conditions) and based on cell survival. We compared the nanoMOF radioenhancement performance to the corresponding equimolar doses of metal oxide nanoparticles (TiO_2, ZrO_2 and HfO_2) in radio-resistant soft tissue sarcoma cells and healthy human fibroblasts. The assessment of the cellular fate and radioenhancement properties illustrated surprising potential for Ti-based nanoMOFs.

Results & discussion

Synthesis and physicochemical characterization of group IV nanoMOFs

We synthesized four different group IV nanoMOFs containing Hf, Ti, and/or Zr metal clusters as radioenhancer candidate materials (Table 1). Hf-DBA and Hf-TCPP have been used for radiation experiments before and can therefore be considered as radioenhancement benchmark materials.[21,24,25] Hf-DBA nanoMOFs, containing $Hf_{12}O_8(OH)_{14}$ clusters linked by 2,5-di(p-benzoato)aniline (DBA), were synthesized based on a pro-

Table 1 Group IV nanoMOF compositions (nanoMOFs colour coded)

nanoMOF	Metal ion	Linker	Theoretical formula	Linker structure
Hf-DBA	Hf^{4+}	2,5-Di(p-benzoato)aniline	$C_{180}H_{149}N_9O_{58}Hf_{12}$	
Hf-TCPP	Hf^{4+}	Porphyrine-tetra-carboxylic acid	$C_{192}H_{124}N_{16}O_{40}Hf_6$	
Ti-MIL-125	Ti^{4+}	2-Aminoterephtalic acid	$C_{48}H_{34}N_6O_{36}Ti_8$	
Ti/Zr-PCN-415	Ti^{4+}, Zr^{4+}	Terephtalic acid	$C_{144}H_{96}O_{108}Ti_{10}Zr_4$	

cedure adapted and scaled up from Ni *et al.*[21] Similarly, Hf-TCPP nanoMOFs, composed of $Hf_6O_4(OH)_4$ clusters linked by tetrakis(4-carboxyphenyl)porphyrin (TCPP), were prepared based on scaled up and adapted protocols from Bao *et al.* and Chen *et al.*[24,25] Additionally, Ti and Ti/Zr based nanoMOFs were synthesized. Ti-MIL-125 has been previously exploited for sensing and catalysis, due to its low bandgap energy, and therefore efficient electron transfer from the linker to the Ti^{4+} center under UV irradiation. The Ti-MIL-125 was synthesized based on a procedure adapted from Vilela *et al.*[26] They are composed of 8-membered Ti–oxo ring clusters linked by 2-aminoterephtalic acid (NH_2–TA). The structure of Ti/Zr-PCN-415 is similar to Ti-MIL-125 with Ti^{4+} ions partially replaced with Zr^{4+} ions, and the linker devoid of one amino functional group. Ti/Zr-PCN-415 nanoMOFs are composed of $Ti_8Zr_2O_{12}(MeCOO)_{16}$ clusters linked by terephtalic acid (TA) and were previously employed by Yuan *et al.*[27] for water reduction catalysis. Here, the latter nanoMOF was selected with the rationale of unifying strong X-ray absorption and photocatalytic activities.

We investigated the morphology and topology of the as-prepared group IV nanoMOFs using scanning transmission electron microscopy (STEM) (Fig. 1A–D). Hf-DBA nanoMOFs exhibited a disc-shape morphology with a diameter of 99 ± 21 nm and a disc thickness of 32 ± 9 nm. STEM imaging revealed a spherical morphology for Hf-TCPP, with a relatively rough surface, and a diameter of 230 ± 45 nm. Morphologically, Ti-MIL-125 had a rice-grain shape with a mean length of 230 ± 41 nm. The cauliflower-like spherical particles of Ti/Zr-PCN-415 had a mean diameter of 192 ± 38 nm. Next to TEM size analysis (Fig. S1†), we also performed

dynamic light scattering (DLS) measurements (Table S1†). However, as not all types of nanoMOFs exhibited a spherical morphology (and hence the prerequisites for DLS-based sizing are not fulfilled), these measurements can only be taken as an estimate. DLS sizes in ethanol remained well below 300 nm, thus confirming STEM findings. In cell culture medium, agglomeration was observed, however, hydrodynamic diameters remained in the sub-micron range for all nanoMOFs. It is well known that particle size strongly influences intracellular uptake and distribution,[28] with both of them being strong determinants of nanoparticle radio-enhancement performance.[7] Interestingly, Orellana-Tavra *et al.* recently showed that larger nanoMOF particles, such as the ones reported here feature a sub-cellular distribution different from smaller nanoMOF particles (which typically end up in lysosomes), offering potentially new prospects also for drug delivery.[29] Fourier transmission infrared spectroscopy (FTIR) of the as-prepared group IV nanoMOFs proved the successful coordination of the linker to the metal clusters through weakening or complete disappearance of the C=O stretch at 1700 cm^{-1}, which is characteristic for carboxylic acid groups (Fig. 1E). Instead, antisymmetric and symmetric COO– stretch modes at 1600 cm^{-1} and 1300 cm^{-1} appeared as a result of the deprotonated linker coordinated to metal centers. FTIR reference spectra are available only for Ti-MIL-125 and are in good agreement with our data.[30] Also, powder X-ray diffraction (XRD) (Fig. 1F) pattern peaks for all group IV nanoMOFs were found well in line with the respective datasets available in literature, hence once again indicating successful nanoMOF synthesis.[21,24,31,32] XRD confirmed crystallinity for Hf-DBA, Hf-
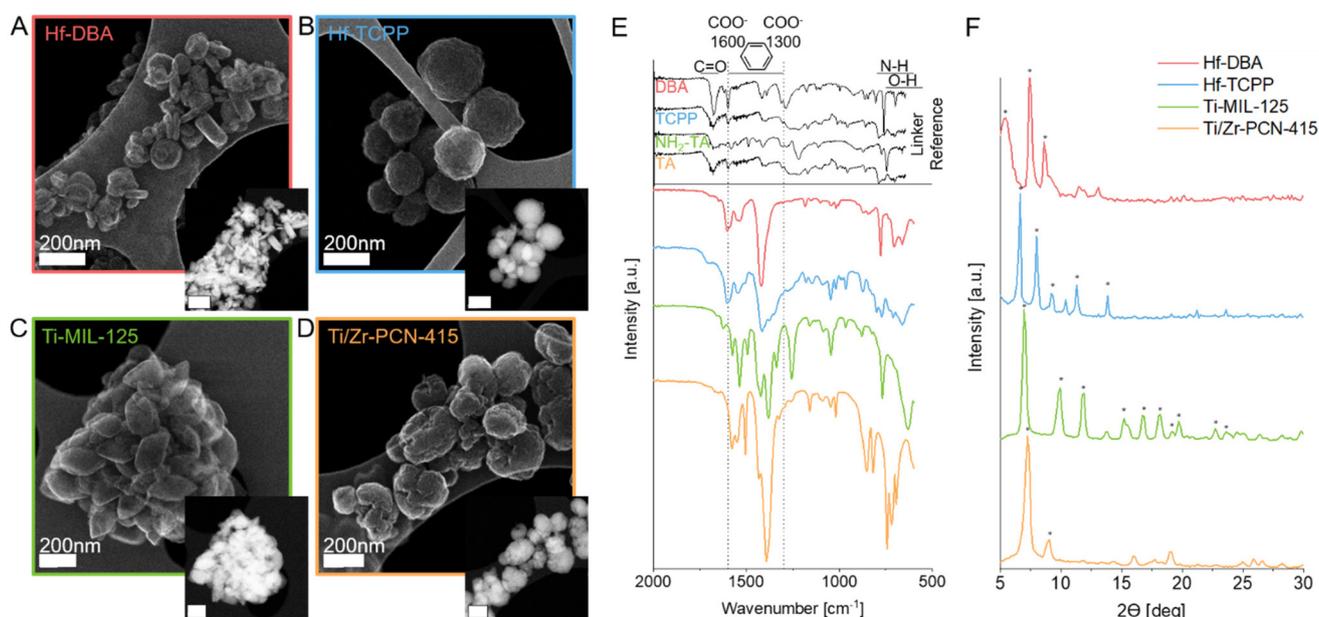

Fig. 1 Secondary electron and HAADF (high angle annular dark field, insets) scanning transmission electron micrographs (STEM) of as-prepared group IV nanoMOFs, including Hf-DBA (A), Hf-TCPP (B), Ti-MIL-125 (C), and Ti/Zr-PCN-415 (D) (all scale bars 200 nm). FTIR spectra (E) with organic linker references and XRD patterns (F) of respective group IV nanoMOFs, including reference peak locations from Ni *et al.*[21] for Hf-DBA, Chen *et al.*[25] for Hf-TCPP, Vilela *et al.*[26] for Ti-MIL-125 and Yuan *et al.*[27] for Ti/Zr-PCN-415 indicated by symbols (*).

TCPP, Ti-MIL-125, and Ti/Zr-PCN-415. Especially for Hf-DBA, high-resolution STEM images (Fig. S2†) showed highly ordered secondary building units with almost atomic-level resolution. The elemental composition of group IV nanoMOFs was measured by carbon hydrogen nitrogen (CHN) elemental analysis and inductively coupled plasma optical emission spectroscopy (ICP-OES). Measured elemental compositions were in excellent agreement with theoretical compositions for all as-prepared group IV nanoMOFs (Tables S2 and S3†) with recoveries of around 100% for Hf-DBA and Ti/Zr-PCN-415 and slightly lower recoveries of around 90% for Hf-TCPP and Ti-MIL-125. Brunauer–Emmett–Teller (BET) surface area measurements yielded specific surface areas (SSA) of 412 ± 13 $m^2 g^{-1}$ for Hf-DBA, 1136 ± 53 $m^2 g^{-1}$ for Hf-TCCP, 835 ± 33 $m^2 g^{-1}$ for Ti-MIL-125, and 587 ± 15 $m^2 g^{-1}$ for PCN-415 nanoMOFs. These physicochemical characterization results confirm the successful synthesis of the four different nanoMOF radioenhancer candidate materials.

Stability of nanoMOFs in buffer environments

Prior to cell culture experiments, and due to the expected lower chemical stability of nanoMOFs compared to their metal oxide counterparts, we investigated the buffer stability of the group IV nanoMOFs by assessing the elemental composition of the solid and soluble fractions after 24 h immersion in different media at 37 °C, respectively (Fig. 2, also see Fig. S3†). The solid fraction was defined as the fraction collected after high-speed centrifugation; whereas the respective supernatant is referred to as the soluble fraction. Hf-DBA were perfectly stable in water and PBS with almost 100% of the Hf recovered as part of the solid fraction and less than 1% of Hf found in the supernatant. However, when exposed to the lysosomal buffer instead, again for 24 h, a fraction of 10.7% (lysosomal buffer pH 4.5) and 8.5% (lysosomal buffer pH 5.5) Hf was found in the soluble fraction. Both Hf-containing nanoMOFs showed similar buffer stability with a slightly higher metal release of 3.5% (compared to <1% for Hf-DBA) into the soluble fraction after water incubation for Hf-TCPP. Also, Ti-MIL-125 nanoMOFs were stable in water and PBS (≤0.1% and ≤2.4% in soluble fraction respectively), however, nearly quantitatively dissolved in lysosomal buffer with below 2% metal remaining in the solid fraction after 24 hours nanoMOF immersion. Again, Ti/Zr-PCN-415 nanoMOFs were fully stable in water whereas in PBS and under lysosomal conditions partial metal release was found. For Ti/Zr-PCN-415, more than 85% of both metals remained in the solid fraction after 24 h immersion in
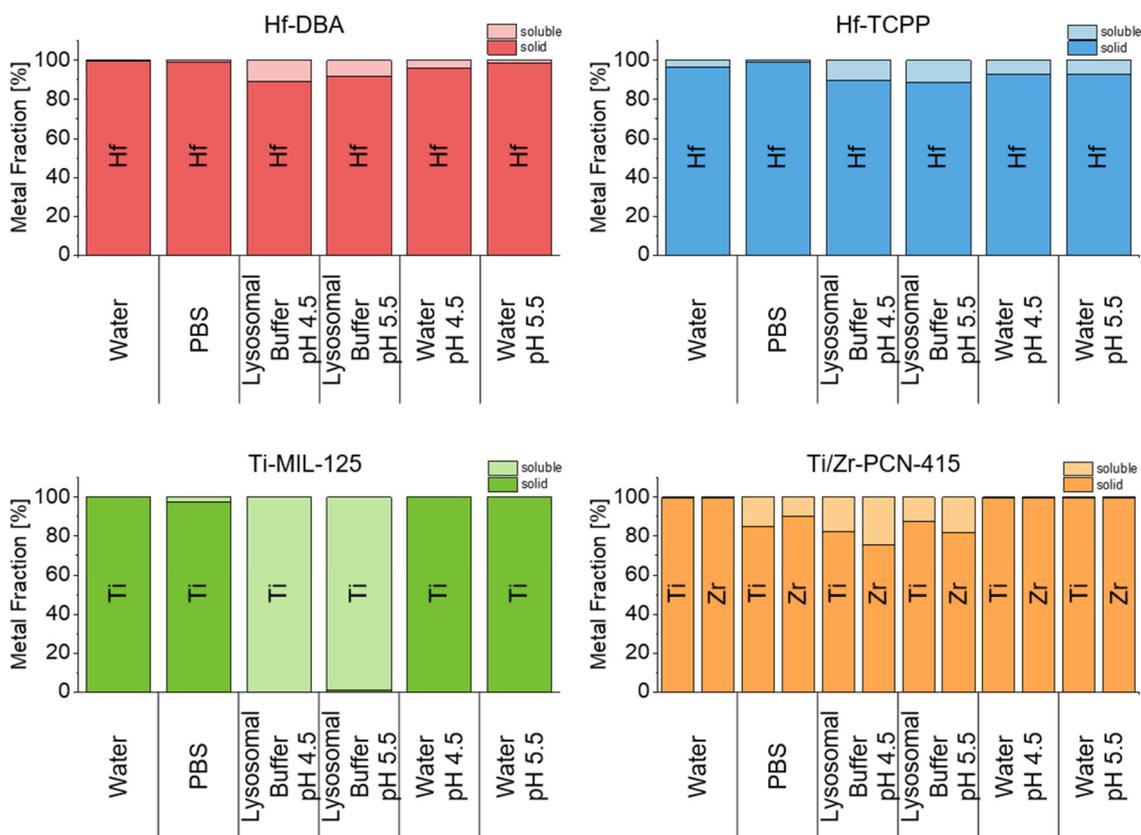

Fig. 2 Metal content in the solid and soluble phase for group IV nanoMOFs exposed to de-ionized water, phosphate buffered saline (PBS), lysosomal buffer (pH 4.5 and 5.5) and HNO₃ acidified water (pH 4.5 and 5.5), respectively, for 24 h at 37 °C and for a nanoMOF concentration of 1 mg mL⁻¹. Metal concentrations of Hf, Zr, Ti were determined by ICP-OES in the soluble and solid fraction of nanoMOF dispersions after separation by high-speed centrifugation.

PBS. This number decreased to 82.4% and 87.4% for Ti and 75.6% and 81.8% for Zr in lysosomal buffer conditions at pH 4.5 and pH 5.5 respectively.

As the lysosomal buffer contains citrate, which might chelate metal ions thus accelerating dissolution, we additionally analyzed the nanoMOF stability in acidified water (containing HNO_3) at pH 4.5 and 5.5, respectively. In both Hf containing nanoMOFs, Hf was released into the soluble fraction with 4.0% and 1.4% for Hf-DBA and 7.4% and 7.5% for Hf-TCPP in acidified water at pH 4.5 and 5.5, respectively, confirming a pH-dependent metal release. In contrast, for both Ti containing nanoMOFs below 1% metal was found in the soluble fraction independent of nanoMOF and pH. (Amino-)terephtalic acid linker nanoMOFs seem thus to be less prone to pH-induced dissolution than DBA and TCPP, however, Ti and Zr ions are chelated by citrate more than Hf ions. With regard to simulating the nanoMOF degradation in acidic compartments, these experiments showed that the nanoMOF stability was higher in acidic water compared to lysosomal buffer at the respective pH for all materials, indicating that in lysosomal buffer not only pH plays a role in dissolution but also citrate as a chelator.

Taken together, these data show that all group IV nanoMOFs are stable with above 96% metal content found in the solid fraction when exposed to water and PBS, except for Ti/Zr-PCN-415 with slightly diminished stability in PBS. Lysosomal conditions simulated by citrate buffer (pH 4.5 and 5.5) led to the highest metal release with either partial (Hf-DBA, Hf-TCPP, and Ti/Zr-PCN-415) or quantitative (Ti-MIL-125) nanoMOF dissolution. The higher metal release in lysosomal buffer compared to PBS, water and acidified water may not only be caused by the acidic environment, but also by the chelation of metal ions by citrate.[33] Taken together, these buffer stability data indicate that all group IV nanoMOFs were stable in physiological buffers, however, are prone to (partial) degradation in acidic environments.

NanoMOF-catalyzed reactive oxygen species generation under irradiation

Due to the importance of reactive oxygen species (ROS) in radio-enhancement, the ability of the nanoMOFs to generate ROS was quantified in a cell-free assay using a DCF (di-chloro-di-hydro-fluorescein) fluorescent assay (Fig. S4†), with high sensitivity for hydroxyl radicals (HO˙). Based on the DCF signal change, dose enhancement factors (DEF) relative to nanoparticle-free controls were highest for Hf-TCPP nanoMOFs. As expected, all nanoMOFs showed a dose-dependent DEF increase, but interestingly, in comparison to respective equimolar oxide nanoparticles (HfO_2, ZrO_2, and TiO_2, see Fig. S5† for characterization data), only Hf-TCPP outperformed HfO_2. All other oxide nanoparticles showed even higher DEFs at equimolar concentrations. This is surprising as it is expected that in an equimolar dosed experiment due to the large surface area in nanoMOFs the number of accessible metal atoms would be higher than in respective metal oxide nanoparticles. As the Hf-TCPP nanoMOFs with the largest linker

and therefore the expectedly biggest pore size performed best, this might indicate a potential limitation in diffusion time of the fluorescent dye into the framework structure and therefore the assay may not account for all ROS effectively generated. Also, the chemical environment, including the buffer system and the cellular system, strongly influences ROS production. Moreover, many of the available fluorescent dye-based ROS quantification assays including the ones available for other H_2O_2 and superoxide anions, are prone to assay interferences[34] (that cannot easily be overcome by nanomaterial removal by centrifugation or precipitation).[35] Thus, the development of alternative methods for ROS quantification is warranted in order to be able to gain additional mechanistic insights.

Cytocompatibility and cellular uptake

Following physicochemical characterization, buffer stability, and ROS generation capability assessment of the as-synthesized group IV nanoMOFs, we investigated mammalian cell compatibility and cellular uptake, as high cell-compatibility is imperative for further radiation enhancement experiments and safe prospective clinical application. We performed short-(Fig. 3A) and long-term (Fig. 3B and C) cytotoxicity studies to assess acute toxicity after 24 h and potential delayed toxicity due to the limited nanoMOF stability (after 5 days) based on a metabolic activity assay (ATP quantification assay). Short-term cytotoxicity in human sarcoma cells (HT1080) (Fig. 3A) showed the lowest impact on viability for Hf-DBA even for high concentrations (250 µg mL^{-1}). In contrast, Hf-TCPP nanoMOFs showed up to 80% viability reduction for the highest dose with a clear dose-dependent viability reduction. The high toxicity for Hf-TCPP nanoMOFs is likely caused by the porphyrin linker, as porphyrins are known for their toxicity in photo-dynamic therapy applications.[36] The two Ti-based nanoMOFs, Ti-MIL-125 and Ti/Zr-PCN-415, showed comparable cytotoxicity effects on HT1080 cells with a dose-dependent viability reduction of around 40% for the highest concentration (250 µg mL^{-1}). Due to their similarity in composition with the linker molecule only differing in one amino group, the similar toxicity profile is not unexpected. Toxicity might be caused by free metal ions after intracellular nanoMOF degradation.[37]

To further evaluate long-term toxicity, which becomes relevant for the radio-enhancement investigation with an overall observation period of 5 days, we investigated the long-term biocompatibility of two sub-toxic group IV nanoMOFs concentrations (4 and 40 µg mL^{-1}) after 5 days in HT1080 cells (Fig. 3B) and normal human dermal fibroblasts (NHDF) (Fig. 3C). The latter served as a non-cancerous control in radio-enhancement studies. For both cell types, no drastic group IV nanoMOF long-term cytotoxicity was observed, except for the Hf-TCPP nanoMOFs which showed a viability reduction of almost 100% for the higher dose (40 µg mL^{-1}). Notably, this dose showed no significant viability reduction in the short-term experiment, however, led to almost complete cell death after 5 days, thus highlighting the importance of assessing long-term effects. In contrast, the slightly diminished viability observed for the higher concentration of the Ti/Zr-PCN-415
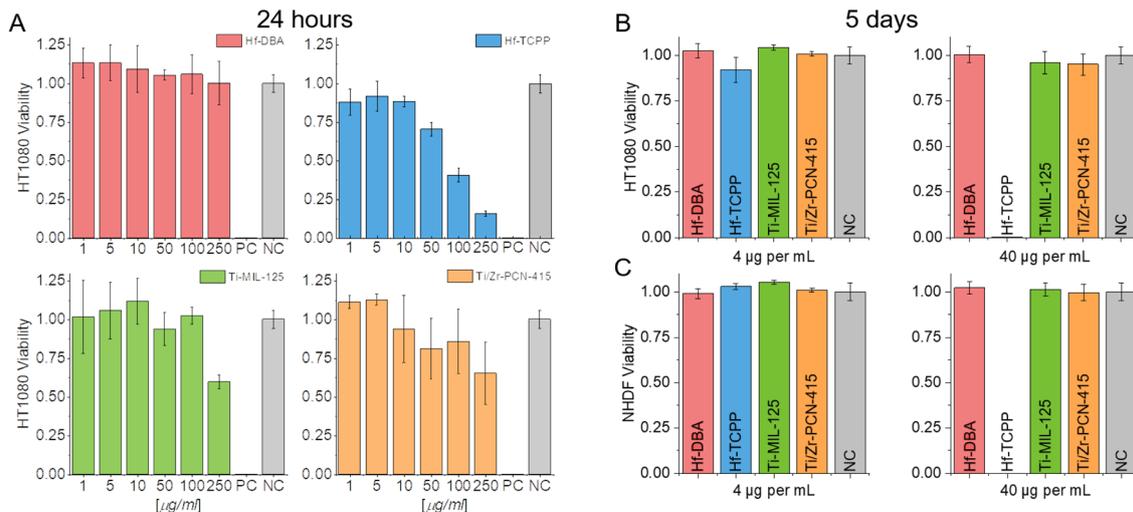
Fig. 3 Short-term (A) cytocompatibility of as-prepared nanoMOFs towards human sarcoma cells (HT1080) after 24 h nanoMOF incubation. Corresponding long-term cytocompatibility in (B) HT1080 sarcoma cells and (C) normal human dermal fibroblasts (NHDF) 5 days after 24 h nanoMOF incubation. Data shown are mean and standard deviation (n = 3).

nanoMOFs during short-term exposure recovered to values comparable to the untreated controls at 5 days, indicating a transient nature of this effect. The distinct differences in long-term toxicity between Hf-TCPP and Ti/Zr-PCN-415, leading in one case to complete cell death, and in the other to full recovery may be explained by the fact that Ti/Zr-PCN-415 were significantly better tolerated than Hf-TCPP at the highest concentrations, which might be reached over time due to sedimentation and continuous uptake. Additionally, the cell response to an initial trigger and the proliferation rate is a highly dynamic and multifactorial process.[38,39]

To be able to contextualize radiation enhancement data, we assessed cellular uptake with ICP-OES (Fig. 4A and B) for metal content quantification and transmission electron microscopy (TEM) imaging (Fig. 4C) for intracellular distribution of the group IV nanoMOFs. We assessed uptake in metal mass per cell in both HT1080 (Fig. 4A) and NHDF (Fig. 4B) cells indicating a comparable nanoparticle uptake (see also Fig. S6† for particle mass per cell). A higher intracellular metal content was found in group IV nanoMOF treated cells compared to oxide nanoparticles (HfO_2, ZrO_2, and TiO_2, see Fig. S5† for characterization data) administered at equimolar metal doses, which can likely be attributed to the smaller size and correspondingly lower sedimentation[40] rate of the metal oxide nanoparticles. While the uptake was relatively comparable for the different types of nanoMOFs at equivalent doses, uptake in all particle-treated samples was cell type- and particle-dose dependent. The overall uptake in NHDF cells for group IV nanoMOFs was slightly lower compared to the uptake in HT1080 cells. Uptake for Hf-DBA into cancerous cells has previously been quantified by the Lin group[21] and is in close agreement with our data. To analyze the nanoMOF intracellular fate, we assessed the uptake of group IV nanoMOFs in HT1080 cells based on TEM imaging (Fig. 4C). As expected, after 24 h incubation, group IV nanoMOFs were inter-

nalized by the cells and localized mainly in vesicular compartments, such as endosomes and lysosomes.[41] NanoMOFs were found partially agglomerated inside these vesicular compartments. After 24 h nanoMOF incubation with HT1080 sarcoma cells, Hf-DBA appeared stable, which was well in line with the buffer stability results (Fig. 2), where over 80% of Hf was found in the solid phase after lysosomal buffer incubation. The stability is also in line with data by Ni *et al.*, who found that Hf-DBA nanoMOFs were stable in cell culture medium over at least 72 h.[21] For Hf-TCCP and Ti/Zr-PCN-415 some pronounced intracellular nanoMOF aggregation and compaction was observed. Ti-MIL-125 appeared morphologically largely unchanged. These results are in line with the buffer stability investigations.

Radio-enhancement performance of group IV nanoMOFs compared to metal oxides

After confirming and quantifying group IV nanoMOF uptake and identifying sub-toxic concentrations (4 μg mL^{-1} Hf-TCPP and 4 and 40 μg mL^{-1} for all other nanoMOFs), we assessed their radio-enhancement efficacies for the aforementioned concentrations in HT1080 and NHDF cells. The survival fraction was assessed five days after irradiation with X-rays (150 keV, Fig. 5) for the nanoMOFs and the corresponding metal oxide nanoparticles at equimolar doses. Survival fractions showed radio-enhancement effects in human sarcoma cells (HT1080), which were strongly dependent on nanoMOF type and dose (Fig. 5A and B for high and Fig. S7† for low nanoMOF concentrations). In sarcoma cells, Hf-based nanoMOFs (Fig. 5A and D) showed dose modifying ratios ($DMR_{50\%}$) of 1.36, which was higher than the HfO_2 nanoparticles with a $DMR_{50\%}$ of around 1.1. These findings indicate the same trend found by Ni *et al.*,[21] however with a lower overall magnitude. Ni *et al.* showed more pronounced effects
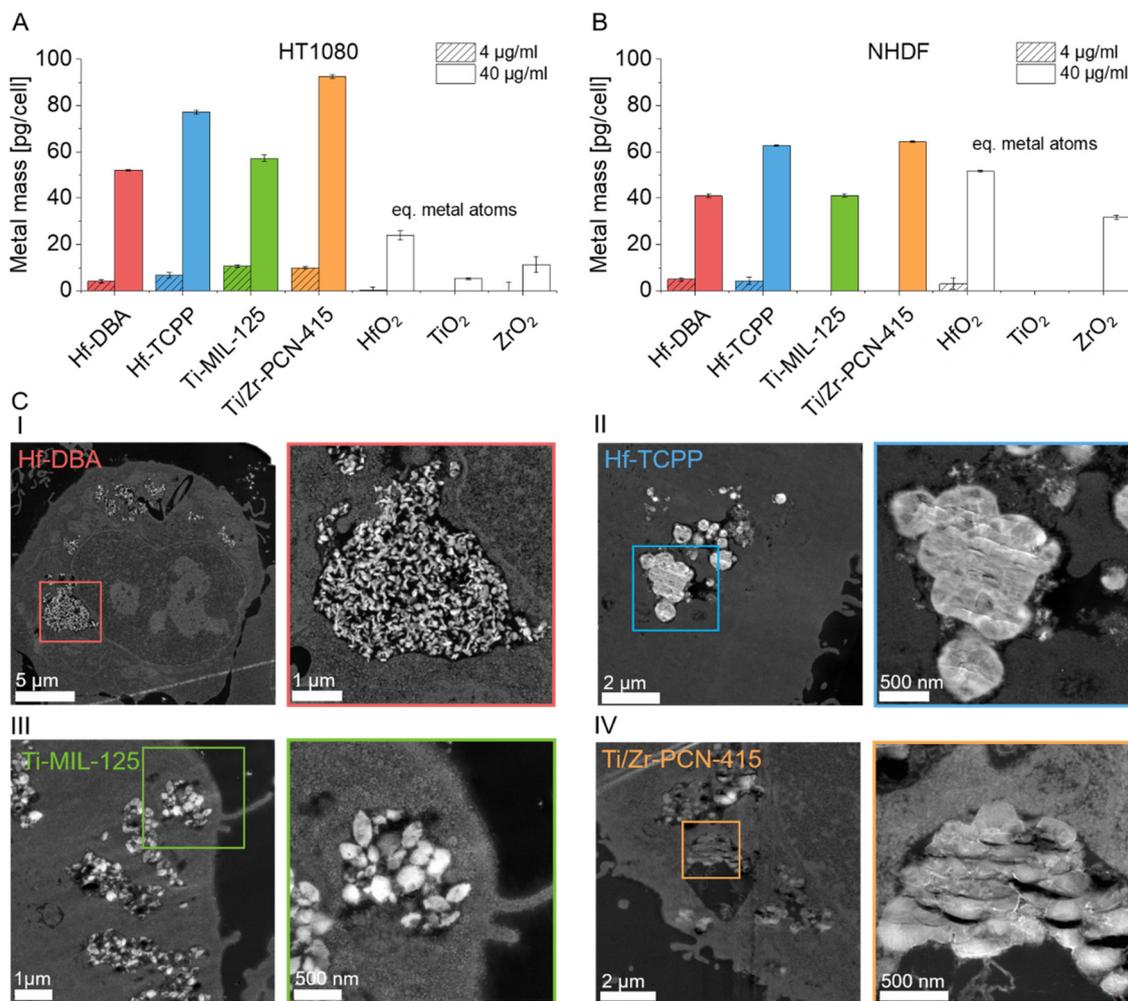
Fig. 4   Metal mass measured by ICP-OES in HT1080 (A) and NHDF (B) cells after 24 h exposure of group IV nanoMOFs and corresponding equimolar dosed metal oxide nanoparticles at two sub-toxic nanoMOF concentrations. High-angle annular dark-field (HAADF) STEM images (C) of Hf-DBA (I), Hf-TCPP (II), Ti-MIL-125 (III), and Ti/Zr-PCN-415 (IV) in HT1080 cells after 24 h nanoMOF administration (40 µg mL^{-1}) showing intracellular nanoMOFs.

with DMR$_{50\%}$ for Hf$_{12}$-DBA of 1.8–3.5 and for equimolar HfO$_2$ of 1.1–2.4 for different cell lines (none of the cell lines studied by Ni *et al.* were HT1080 cells).[21] Interestingly, in our study, we found that a 10-fold lower concentration of Hf-TCPP (4 µg mL^{-1}) performed almost identical to Hf-DBA (40 µg mL^{-1}) with DMR$_{50\%}$ of 1.36 and 1.37 respectively (Fig. 5D). This can only partially be explained by the larger specific surface area of Hf-TCPP (3× higher compared to Hf-DBA) and indicates a significant role of other parameters, including the particle size, surface roughness, linker molecule, *etc*. In contrast to Hf-MOFs, Ti-based nanoMOFs (Fig. 5B and D) strongly outperformed the corresponding equidosed oxide nanoparticles *in vitro* with DMR$_{50\%}$ values of 3.8 in Ti-MIL-125 and 2.2 in Ti/Zr-PCN-415 compared to 0.9 for ZrO$_2$ and 1.2 for TiO$_2$. Again, for the low nanoMOF doses (Fig. S6†), no significant enhancement effects were found. Table S4† summarizes DEF$_{8Gy}$, DMR$_{50\%}$, and LD$_{50}$ values for all nanoMOFs, oxide nanoparticles, and concentrations investigated.

Generally, all Ti-containing particles presented higher DMR$_{50\%}$ compared to the Hf-based materials. This illustrates that high atomic number alone is not the only determinant for a high radio-enhancement capability (in line with DCF findings, see Fig. S4†),[42] but other factors, such as catalytic activity, may also play an important role.[43] Indeed, the material with the highest atomic number (Hf-DBA) investigated here, presented the lowest DMR$_{50\%}$ values at uptake levels comparable to the other nanoMOFs. In contrast, Ti-MIL-125 with a lower atomic number (compared to Hf-based materials), presented the highest DMR$_{50\%}$ in this study, strengthening the hypothesis of catalytic activity through electron transfer from the linker to the metal might impact the radiation enhancement.[30,44] The higher ROS generation in Ti-based materials could partially be explained by a radical generation through a pseudo-Fenton reaction, which is known for titanium active sites.[45,46] A linker excitation followed by a linker-mediated metal reduction of Ti^{4+} to Ti^{3+}, might lead to an
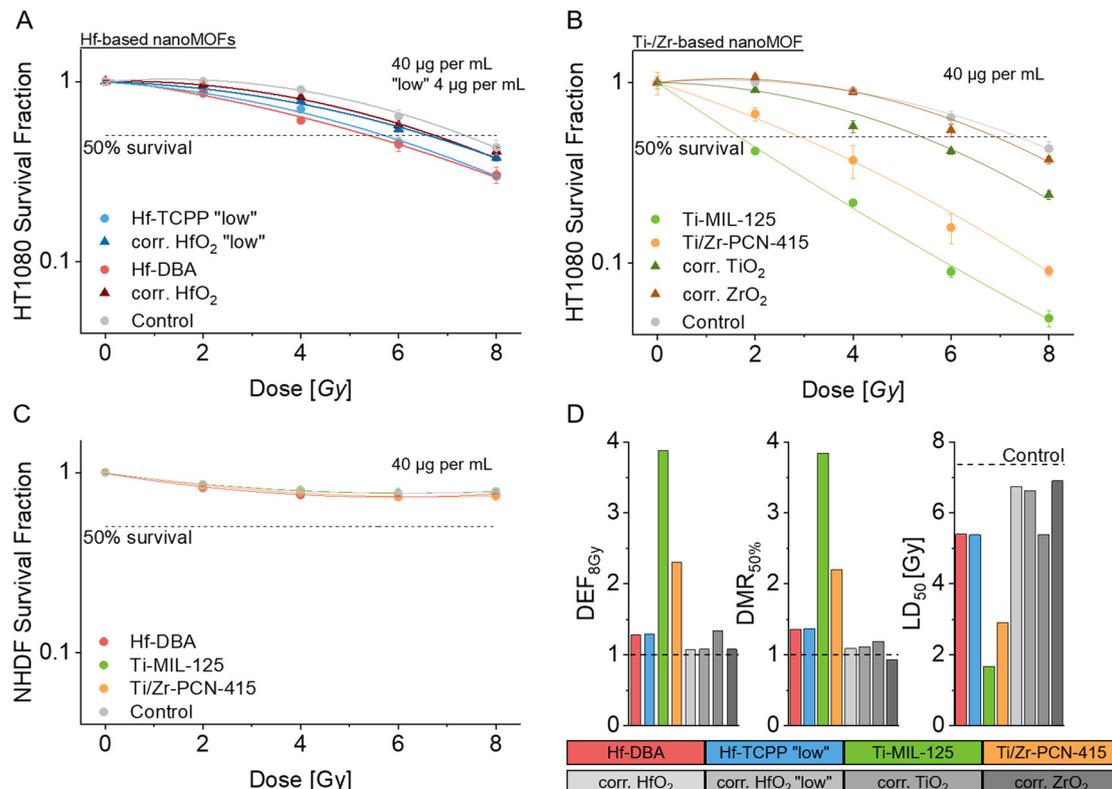
Fig. 5 Radioenhancement in HT1080 for (A) Hf-based nanoMOFs and equi-dosed HfO$_2$ nanoparticles and (B) Ti-/Zr-based nanoMOFs and equi-dosed TiO$_2$ and ZiO$_2$. Radioenhancement in NHDF cells (C) for all nanoMOFs. Treatment doses at 40 μg mL^{-1} or 4 μg mL^{-1} labelled as "low" (corresponding to 10 and 1 ng per cell) were used. (D) Dose enhancement factor (DEFs) at 8 Gy radiation, dose modifying ratio (DMR) at 50% survival and the 50% lethal dose (LD) for HT1080 cells. Data shown are mean and SD (n = 3).

overall better performance of Ti-based nanoMOFs compared to Hf-based materials as seen in this study. A possible catalytic cycle includes a pseudo-Fenton reaction mechanism for switching from Ti^{4+} to Ti^{3+} as proposed in parts by Liu *et al.*[45] for TiO$_2$ and electron transfer from the linker to the metal (Fig. S8†). While in this work, we have employed as-synthesized Ti-MIL-125, interestingly, recent research in photocatalysis has demonstrated that the activity of Ti-MIL-125 may be boosted even further by oxygen vacancy engineering, *e.g.* using propionic acid as an etching agent.[47,48] It has also been shown that the MOF catalytic activity is crystal facet-dependent; facets containing a higher proportion of the metal clusters on the surface possess a higher activity and surface energy. However, compared to the well-established concept in hard materials, such as metal oxides, crystal facet characterization, and engineering in MOFs requires additional efforts due to the complexity of these soft materials and the coexistence of various types of chemical bonds.[49]

Interestingly, in the non-cancerous NHDF cells, no radio-enhancement effect was detectable, neither for high (Fig. 5C) nor low (Fig. S7†) nanoMOF concentrations, at uptake values comparable between cancerous and non-cancerous cell lines. These findings indicate a higher therapeutic ratio and are in line with previous studies on metal oxide nanoparticles, where considerably lower dose-enhancement efficacies have been

observed in non-cancerous fibroblasts compared to cancerous cells.[42] The better performance of nanoMOFs compared to the corresponding oxides in equimolar conditions can in part be explained by the higher cell internalization of nanoMOFs as well as the higher accessible surface area of nanoMOFs.

Conclusion

With this work, we introduce group IV transition metal nanoMOFs beyond Hf-MOFs as promising radio-enhancers with high therapeutic ratios. Greatest *in vitro* radio-enhancement effects were found for Ti-MIL-125, followed by Ti/Zr-PCN-415 nanoMOFs, confirming that not only high atomic number metals but also catalytic[43] and radioluminescence[50] processes should be considered in the molecular design of high-performance radio-enhancers. While radio-enhancement efficiencies in human sarcoma cells were high, especially for Ti-containing nanoMOFs, they were attenuated to untreated control values in healthy fibroblasts at comparable nanoMOF uptake values, offering new prospects for targeted (tissue-specific) radiotherapy. However, in addition to high radio-enhancement efficiencies, a detailed understanding of stability and intracellular fate is imperative with regard to prospective clinical applications. We show high buffer stability for all

nanoMOFs in water and PBS with less than 20% metal release from the as-synthesized framework whereas in acidic, lysosome-mimicking conditions, nanoMOFs showed partial dissolution. Nonetheless, three out of four nanoMOFs (Hf-DBA, Ti-MIL-125, Ti/Zr-PCN-415) showed high short and long-term cytocompatibility, indicating that gradual stability reduction might even offer new prospects for radio-enhancer clearance. Taken together, the here presented group IV nanoMOFs, especially the Ti-based nanoMOFs, outperformed corresponding equimolar metal oxide nanoparticles in *in vitro* X-ray radio-enhancement and therefore offer promising prospects for nanoMOF-based high-performance radio-enhancement.

Experimental section

NanoMOF synthesis

Hf(IV)-DBA. nanoMOFs were synthesized according to a scaled up version of Lin *et al.*[21] In brief, 160 mg $HfCl_4$ and 160 mg H_2DBA (2,5-di(*p*-benzoato)aniline) were separately stirred in 100 ml DMF for 60 minutes at room temperature (RT). Afterwards, the two solutions were combined and 15 ml acetic acid and 1 ml H_2O was added. The resulting mixture was stirred for additional 10 minutes, after which the stir bar was removed, the flask sealed with a septum and placed in an oven at 80 °C for 72 h. The previously colorless liquid turned turbid and a white/light yellow precipitate was observed. The precipitate was collected by centrifugation at 4 °C with 11 000g for 45 minutes. The precipitate was then washed once with DMF, then once with 1% trimethylamine/ethanol, and then twice with ethanol and finally dried overnight at 40 °C under vacuum.

Hf(IV)-TCPP. nanoMOFs were synthesized following a modified and scaled up procedure previously reported by Lu *et al.*[51] Briefly, 313 mg of TCPP (tetrakis(4-carboxyphenyl)porphyrine) were suspended in 82 ml DMF and stirred for 10 minutes. 200 µl triethylamine was added and the resulting mixture was stirred for an additional 10 minutes. Next, 13.6 ml acetic acid were added and the flask was sealed with a septum. The flask was then immersed in an oil bath set to 115 °C for 45 minutes. Meanwhile 126.7 mg $HfCl_4$ were dissolved in 20 ml DMF at RT. The $HfCl_4$ solution was then injected *via* syringe into the hot mixture containing the porphyrin linker and after stirring for 5 min, the stir bar was removed from the liquid. The reddish/purple-coloured reaction mixture was kept in the oil bath for an additional 6 h. A colour change to a deeper purple was observed. A dark purple precipitate was collected after centrifugation at 4 °C at 11 000g for 45 minutes. The precipitate was washed twice with DMF, then once with 1% triethylamine/ethanol, and then twice with ethanol and finally dried overnight at 40 °C under vacuum.

Ti(IV)-amino-MIL-125. nanoMOFs were synthesized following the procedure published by Horcajada *et al.*[31] In brief, 1.375 g of 2-aminoterephtalic acid (Sigma Aldrich) in 20 ml DMF and 5 ml methanol was vigorously stirred for 40 min in a sealed round bottom flask for homogenous dissolution. The linker solution was heated for 10 min in an oil bath set to 110 °C. Further, 1.5 ml titanium isopropoxide and 100 µl water was added under further continuous vigorous stirring. A colour change from dark yellow to a milky lighter yellow was observed. Heating and stirring was continued for 32 h. The bright yellow reaction precipitate was collected and washed once with DMF and two times with Ethanol (centrifugation 11 000g at 4 °C for 45 min) and finally dried overnight at 40 °C under vacuum.

Ti(IV)/Zr(IV)-PCN-415. nanoMOFs were synthesized following a procedure described by Yuan *et al.*[32] Briefly, 50 mg $ZrCl_4$ in 5 ml DMF was stirred for 5 minutes at RT for complete dissolution. Further, 500 µl acetic acid and 100 µl titanium isopropoide were added under continued stirring for 10 min at RT. The flask was sealed and heated in an oven at 100 °C for 24 h without further stirring. To the precipitate a homogenous solution of 800 mg terephtalic acid in homogeneously dissolved 10 ml DMF was added and stirring was reinitiated. Then, 1 ml trifluoroacetic acid was added and stirred for another 5 min. The solution was transferred into a steel lined Teflon autoclave and placed in an oven at 140 °C for another 24 h. The white precipitate was collected after cooling and washed once with DMF and twice with Ethanol (centrifugation at 4 °C with 11 000g for 45 minutes) and finally dried overnight at 40 °C under vacuum.

Corresponding oxide nanoparticles HfO_2, TiO_2 and ZrO_2 were synthesized *via* flame spray pyrolysis based on procedures reported elsewhere.[42]

NanoMOF characterization

Scanning transmission electron micrographs (STEM) images of as prepared nanoparticles were recorded on a Talos F200X TEM (Super-X EDS, 4 detector configuration, FEI, USA) at an acceleration voltage of 200 kV. NP samples were prepared *via* a drop through grid method of 1 mg ml^{-1} nanoMOF suspension in ethanol on nickel (Hf-DBA; Hf-TCPP)/copper (Ti-MIL-125; Ti/Zr-PCN-415) grids (EMR, Holey Carbon Film 200 Mesh Nickel/Copper). NanoMOF suspension was placed on the respective grid for 2 min and pulled through the grid with a filter paper, the grid was then washed three times with water.

Fourier transform infrared spectroscopy (FTIR) measurements were performed using a Varian 640 IR FT-IR spectrometer. Transmission of samples were measured in solid form and previously measure background subtracted.

X-ray diffraction (XRD) patterns were obtained using a Bruker D2 Phaser (30 kV, mA). Dry MOF sample were measured at the diffraction angle 2θ from 5° to 50° in 0.15° per step.

Dynamic light scattering (DLS) hydrodynamic size measurements were obtained using a Zetasizer Nano ZS90 (Malvern Instruments Ltd, Worcestershire, United Kingdom) with a 90° scattering angle. To assess dispersant effects on hydrodynamic size, particles were dispersed in water, ethanol and cell culture medium at a concentration of 1 mg mL^{-1}. The 1 mg ml^{-1} stock solutions were diluted dependent on the particle from

$0.1–0.9 \text{ mg mL}^{-1}$ to ensure a count rate between 200–400 kcps at an attenuator level of 7–9.

Inductively coupled plasma optical emission spectrometry (ICP-OES) measurements of 1 mg ml^{-1} nanoMOFs dispersion in water. 500 µl of sample were mixed with 1500 µl sulfuric acid (H_2SO_4) and 1500 µl ultrapure water in a quartz digestion tube. For digestion, a pressurized microwave (turboWAVE I500 MWS GmbH, Germany) at 1000 W, 200 °C and 150 bar pressure for 40 minutes was used. After digestion in the microwave, 1000 µl hydrogen peroxide (H_2O_2) was added to each sample, carefully mixed and allowed to react for 20 minutes. The tube contents were then transferred to 50 ml falcon tubes and filled to the 25 ml mark with 2% nitric acid (HNO_3). To verify the adequacy of this digestion method, each nanoMOF was also digested once using the gold standard method, where 500 µl of sample were mixed with 1 mL 40% hydrofluoric acid (HF) in 3 ml HNO_3 and digested in a pressurized microwave as above. Recoveries of the sulfuric acid method were at 95–98% of the content determined using the HF method, which were considered 100%. The respective metal content was quantified using an Agilent 5110 ICP-OES (Agilent, Switzerland) with external calibration from 0 to 5 ppm.

Brunauer–Emmett–Teller (BET) method was used for specific surface area analysis by a five-point N_2 adsorption isotherm measurement at 77 K after degassing for 2 h at 180 °C using a Micromeritics Tristar II PLUS.

Cell-free experiments

Buffer stability. For nanoMOF buffer stability, 1 mg ml^{-1} nanoMOF dispersion in respective fluids (water, PBS and lysosomal buffer (10 mM citrate buffer) at pH 4.5 and 5.5) were prepared through bath sonication with total volume of 10 mL for 20 min. nanoMOF suspensions were incubated at 37 °C in an overhead rotator for 24 h. All nanoMOF suspensions were well sonicated for homogeneous sampling. For the total fraction 1 ml of the homogeneous dispersion was collected and after centrifugation at 11 000g for 45 min the supernatant was collected as soluble fraction. After washing twice with water the residual solid was dispersed in 0.9 ml water as solid fraction and considered as a concentration of 10 mg ml^{-1} (as 1 ml was removed for total fraction). For total and soluble fraction 250 µl and 50 µl for solid fraction were digested with 750 µl H_2SO_4 and 750 µl water in pressurized microwave. After microwave digestion 500 µl H_2O_2 were added and allowed to react for 20 min before transfer to 50 ml tube and filled to 25 ml mark with 2% HNO_3. The respective metal content was then quantified using an Agilent 5110 ICP-OES (Agilent, Switzerland) with external calibration from 0 to 5 ppm.

Dichlorodihydrofluorescein assay (DCF). Cell free dose enhancement of nanoMOFs for ROS generation was measured using a 2,7-dichlorodihydrofluorescein diacetate ($H_2DCF-DA$) assay adapted from a procedure published by Zhao et al.[52] Maximum 2 h prior irradiation 10 mg ml^{-1} nanoMOF dispersion in water was prepared and diluted in 0.1 M triethylammonium acetate buffer (TEA-buffer, pH 7) to desired concentrations and kept on ice for transportation. Prior to

irradiation samples were equilibrate to RT for 20 min. A DCF working solution was prepared by activation of 90 µl pre-DCF (5 mM $H_2DCF-DA$, in dimethyl sulfoxide) with 360 µl NaOH. Then, 360 µl of the resulting highly reactive deprotonated and deacetylated DCF-working solution was diluted with 44.64 mL TEA-buffer and protected from light. For irradiation 24-well plates were used with nanoMOF concentrations ranging from 1 to 500 µg mL^{-1} including buffer blank and respective non-irradiated controls. Each well contained 200 µl particle dispersion and 800 µl DCF working solution resulting in a total volume of 1 mL. As radiation source a 150 keV SEIFERT X-ray Tubehousing ISOVOLT 420/10 (SEIFERT) operating at 20 mA equipped with a Thoreaus1 filter was used. Samples were irradiated with 12 Gy at a dose rate of 1.44 Gy min^{-1}. After irradiation the irradiated as well as the non-irradiated samples was transferred to 2 ml Eppendorf tubes and centrifuged at 21 000g at 4 °C for 5 min. Then, 500 µl supernatant was transferred to a new tube without nanoMOF contamination and stored on ice for transportation. Technical triplicates of 150 µl each sample were transferred to a clear bottom 96 well plate and fluorescence was measured at an excitation wavelength of 485 nm and an emission wavelength of 528 nm at 40% lamp energy using a Mithras LB 943 Multimode plate reader. The dose enhancement factor DEF was calculated as:

$$\text{DEF} = \frac{(f_{12S} - f_{0S})}{(f_{12C} - f_{0C})}$$

where f_{12S} stands for the mean fluorescence intensity of the 12 Gy irradiated nanoMOF containing sample and f_{12C} for the respective 12 Gy irradiated particle free control. Similarly, f_{0S} and f_{0C} indicates the respective non-irradiated sample and control.

In vitro experiments

Cell handling. HT1080 (human fibrosarcoma) cell line was obtained from ATCC and NHDF (normal human dermal fibroblast) primary cells were obtained from PromoCell. The HT1080 cell line was cultured in Minimum Essential Medium Eagle (MEM, Sigma) supplemented with 10% Fetal Calve Serum (FCS, Sigma-Aldrich), 1% L-glutamine (Sigma-Aldrich), 1% Penicillin–Streptomycin (PS, Sigma-Aldrich), and 1% non-essential amino acids (Sigma-Aldrich) full growth medium. NHDF cells were cultured in Dulbecco's Modified Eagle's Medium-high glucose (Sigma-Aldrich) supplemented with 10% Fetal Calve Serum (FCS, Sigma-Aldrich), 1% L-glutamine (Sigma-Aldrich), and 1% Penicillin–Streptomycin (PS, Sigma-Aldrich) full growth medium. Cells were sub-cultured upon 80% confluence and cultured in a humidified incubator at 37 °C under 5% CO_2 atmosphere (standard culture conditions).

Cytotoxicity. For viability assessment CellTiter-Glo® Luminescent Cell Viability Assay (Promega, Switzerland) was used for ATP quantification.[53] Briefly, 5000 HT1080 or NHDF cells were seeded in 100 µl full growth medium in black clear bottom 96-well plates and allowed to attach overnight. NanoMOF treatment was performed in triplicates at concentrations ranging from $1–250 \text{ µg ml}^{-1}$ (corresponding to 0.2–50 ng per cell). NanoMOF suspensions were diluted in respective

cell culture medium from a 10 mg mL^{-1} stock(in water). Cells were incubated with nanoMOFs for 24 h and washed twice with PBS. For short-term cytotoxicity viability was assessed directly after nanoMOF removal or after 5 days for long term toxicity. For positive control cells were lysed with 10 μL 1% Triton-X. CellTiter-Glo® assay was performed according to the manufacturer protocol with 50 μL fresh medium and 50 μL reagent. Plate was shock for 30 min and 10 min signal equilibration was allowed prior luminescence determination using a Mithras LB 943 Multimode plate reader.

Quantitative cellular uptake. For cellular nanoMOF and particle uptake 25 000 HT1080 or NHDF cells were seeded in 12-well plates, allowed to attach overnight and treated with 4 or 40 μg mL^{-1} (total volume 1 mL) nanoMOF and respective metal-mass equi-dosed oxide particle in cellculture medium. After 24 h incubation remaining nanoMOFs/particle were removed and cells washed two times with PBS for extracellular nanoMOF removal. Cells were detached with trypsin, counted and 10 000 cells per sample were pelleted by 5 min centrifugation at 200g. Matrix free cells were digested and further procedure as described above in the ICP-OES section. The respective metal content was then quantified using an Agilent 5110 ICP-OES (Agilent, Switzerland) with external calibration from 0 to 5 ppm.

Electron microscopy of nanoMOFs in cells. For STEM *in vitro* sample preparation, cells were seeded and treated as in the quantitative cellular uptake section (4.4.3) above and after nanoMOF removal and washing with PBS treated as follows. Cells were fixed in well with 2.5% glutaraldehyde in 0.1 M sodium cacodylate buffer for 1 h at RT followed by washing twice with 0.1 M sodium cacodylate buffer for 3 min. Samples were stained with 1% osmium tetroxide in 0.1 M sodium cacodylate buffer for 1 h at RT protected from light. Three times washing for 3 min with water was followed by subsequent ethanol dehydration (30%, 50%, 70%, 90% ethanol) 5 min each and three times 10 min with 100% ethanol. Finally the samples were embedded in Epon (1 h ethanol : Epon 1 : 1 RT, overnight 100% Epon with open lid RT) and finally polymerized in fresh 100% Epon at 60 °C for 48 h. Sections of 60 nm thickness were cut and STEM images recorded on a Talos F200X TEM (Super-X EDS, 4 detector configuration, FEI, USA) at an acceleration voltage of 200 kV.

In vitro irradiation enhancement. Cells were seeded in 300 μl full growth medium into 48-well plates at a density of 2000 cells per well for HT1080 and 5000 cells per well for NHDF cells and allowed to attach. Different cell densities were chosen according to their doubling time. On the following day, cells were treated by adding 200 μl particle suspension resulting in a final volume of 500 μl per well and a final concentration of 4 or 40 μg mL^{-1}. Respective metal oxide nanoparticles were treated in an equi-dosed metal mass concentration. Generally, experiments were performed in triplicates. After 24 h treatment, the particles were removed and samples washed twice with PBS and replaced with fresh medium. For transportation cell were kept on ice for no longer than 1 h. Before irradiation cells were allowed equilibrate to RT for 20 min. As a radiation source a 150 keV SEIFERT X-ray

Tubehousing ISOVOLT 420/10 (SEIFERT) operating at 20 mA equipped with a Thoreaus1 filter was used. Additionally a 6 cm thick Perspex plate functioned as a water phantom to simulate more reliable biological conditions and a 12 mm thick aluminum plate was used to increase beam hardening. Irradiation doses of 0–8 Gy were applied with a dose rate of 0.6 Gy min^{-1}. Viability, using the CellTiter-Glo® assay as described above, was assessed 5 days post irradiation, when particle free 0 Gy irradiation control cells reached confluence.

The dose enhancement factor[54] ($DEF_{x Gy}$) was calculated as following:

$$DEF_{x Gy} = \frac{x Gy_{control}}{Gy_{sample} \text{ required for identical SF}}$$

with $x Gy_{control}$ for the survival fraction of particle free sample at given irradiation dose and Gy_{sample} required for identical SF for the respective required irradiation dose needed to achieve the same survival fraction (SF) for particle treated sample.

The dose modifying ratio[54] (DMR) was calculated as following:

$$DMR_{SF} = \frac{x Gy_{P \text{ at } y SF}}{x Gy_{y SF}}$$

with $x Gy_{y SF}$ for the irradiation dose needed in particle free control for specific SF and $x Gy_{P \text{ at } y SF}$ for irradiation dose in particle treated sample. According to this the lethal dose LD$_{50}$ was calculated with

$$LD_{50} = x Gy_{50\% SF}.$$

Conflicts of interest

There are no conflicts to declare.

Acknowledgements

References

1 H. Krieger and W. Petzold, *Strahlenphysik, Dosimetrie und Strahlenschutz*, Vieweg + Teubner Verlag, Wiesbaden, 1992.
2 C. R. Lewanski and W. J. Gullick, *Lancet Oncol.*, 2001, **2**, 366.

3 G. C. Barnett, C. M. L. West, A. M. Dunning, R. M. Elliott, C. E. Coles, P. D. P. Pharoah and N. G. Burnet, *Nat. Rev. Cancer*, 2009, **9**, 134.

4 Y. Matsuno, M. Hyodo, H. Fujimori, A. Shimizu and K. Yoshioka, *Cancers*, 2018, **10**, 364.

5 A. Guerreiro, N. Chatterton, E. M. Crabb and J. P. Golding, *Cancer Nanotechnol.*, 2019, **10**, 10.

6 K. T. Butterworth, S. J. McMahon, F. J. Currell and K. M. Prise, *Nanoscale*, 2012, **4**, 4830.

7 A. L. Neuer, L. R. H. Gerken, K. Keevend, A. Gogos and I. K. Herrmann, *Nanoscale Adv.*, 2020, **2**, 2992.

8 A. Pottier, E. Borghi and L. Levy, *Anticancer Res.*, 2014, **34**, 443.

9 L. Maggiorella, G. Barouch, C. Devaux, A. Pottier, E. Deutsch, J. Bourhis, E. Borghi and L. Levy, *Future Oncol.*, 2012, **8**, 1167.

10 Z. Kuncic, *Phys. Med. Biol.*, 2018, **28**(63), 02TR01.

11 D. Howard, S. Sebastian, Q. V.-C. Le, B. Thierry and I. Kempson, *Int. J. Mol. Sci.*, 2020, **21**, 579.

12 A. Abdal Dayem, M. K. Hossain, S. B. Lee, K. Kim, S. K. Saha, G.-M. Yang, H. Y. Choi and S.-G. Cho, *Int. J. Mol. Sci.*, 2017, **18**, 120.

13 Y.-W. Huang, M. Cambre and H.-J. Lee, *Int. J. Mol. Sci.*, 2017, **18**, 2702.

14 H. Li, M. Eddaoudi, M. O'Keeffe and O. M. Yaghi, *Nature*, 1999, **402**, 276.

15 J. L. C. Rowsell and O. M. Yaghi, *Microporous Mesoporous Mater.*, 2004, **73**, 3.

16 O. M. Yaghi, G. Li and H. Li, *Nature*, 1995, **378**, 703.

17 O. M. Yaghi, M. O'Keeffe, N. W. Ockwig, H. K. Chae, M. Eddaoudi and J. Kim, *Nature*, 2003, **423**, 705.

18 Q. Wang and D. Astruc, *Chem. Rev.*, 2020, **120**, 1438.

19 X. Ma, M. Lepoitevin and C. Serre, *Mater. Chem. Front.*, 2021, **5**, 5573.

20 S. Wang, C. M. McGuirk, A. d'Aquino, J. A. Mason and C. A. Mirkin, *Adv. Mater.*, 2018, **30**, 1800202.

21 K. Ni, G. Lan, C. Chan, B. Quigley, K. Lu, T. Aung, N. Guo, P. La Riviere, R. R. Weichselbaum and W. Lin, *Nat. Commun.*, 2018, **9**, 2351.

22 S. Bonvalot, P. L. Rutkowski, J. Thariat, S. Carrère, A. Ducassou, M.-P. Sunyach, P. Agoston, A. Hong, A. Mervoyer, M. Rastrelli, *et al.*, *Lancet Oncol.*, 2019, **20**, 1148.

23 M. Kleczkowski and M. Garncarz, *Pol. J. Vet. Sci.*, 2012, **15**, 165.

24 J. Bao, X. Zu, X. Wang, J. Li, D. Fan, Y. Shi, Q. Xia and J. Cheng, *Int. J. Nanomed.*, 2020, **15**, 7687.

25 Y. Chen, H. Zhong, J. Wang, X. Wan, Y. Li, W. Pan, N. Li and B. Tang, *Chem. Sci.*, 2019, **10**, 5773.

26 S. Vilela, P. Salcedo-Abraira, I. Colinet, F. Salles, M. de Koning, M. Joosen, C. Serre and P. Horcajada, *Nanomaterials*, 2017, **7**, 321.

27 S. Yuan, J.-S. Qin, H.-Q. Xu, J. Su, D. Rossi, Y. Chen, L. Zhang, C. Lollar, Q. Wang, H.-L. Jiang, *et al.*, *ACS Cent. Sci.*, 2018, **4**, 105.

28 P. Foroozandeh and A. A. Aziz, *Nanoscale Res. Lett.*, 2018, **13**, 339.

29 C. Orellana-Tavra, S. A. Mercado and D. Fairen-Jimenez, *Adv. Healthcare Mater.*, 2016, **5**, 2261.

30 Y. Fu, D. Sun, Y. Chen, R. Huang, Z. Ding, X. Fu and Z. Li, *Angew. Chem., Int. Ed.*, 2012, **51**, 3364.

31 S. Vilela, P. Salcedo-Abraira, I. Colinet, F. Salles, M. de Koning, M. Joosen, C. Serre and P. Horcajada, *Nanomaterials*, 2017, **7**, 321.

32 S. Yuan, J.-S. Qin, H.-Q. Xu, J. Su, D. Rossi, Y. Chen, L. Zhang, C. Lollar, Q. Wang, H.-L. Jiang, *et al.*, *ACS Cent. Sci.*, 2018, **4**, 105.

33 R. Uppal, C. D. Incarvito, K. V. Lakshmi and A. M. Valentine, *Inorg. Chem.*, 2006, **45**, 1795.

34 J. Zhao and M. Riediker, *J. Nanopart. Res.*, 2014, **16**, 2493.

35 S. Zwiehoff, J. Johny, C. Behrends, A. Landmann, F. Mentzel, C. Bäumer, K. Kröninger, C. Rehbock, B. Timmermann and S. Barcikowski, *Small*, 2022, **18**, 2106383.

36 J. Kou, D. Dou and L. Yang, *Oncotarget*, 2017, **8**, 81591.

37 À. Ruyra, A. Yazdi, J. Espín, A. Carné-Sánchez, N. Roher, J. Lorenzo, I. Imaz and D. Maspoch, *Chem. – Eur. J.*, 2015, **21**, 2508.

38 J. Liu, Y. Yang, W. Zhu, X. Yi, Z. Dong, X. Xu, M. Chen, K. Yang, G. Lu, L. Jiang, *et al.*, *Biomaterials*, 2016, **97**, 1.

39 J. Wang, D. Chen, B. Li, J. He, D. Duan, D. Shao and M. Nie, *Sci. Rep.*, 2016, **6**, 26126.

40 A. Spyrogianni, I. K. Herrmann, M. S. Lucas, J.-C. Leroux and G. A. Sotiriou, *Nanomedicine*, 2016, **11**, 2483.

41 S. S. Teske and C. S. Detweiler, *Int. J. Environ. Res. Public Health*, 2015, **12**, 1112.

42 L. Gerken, A. Neuer, P. Gschwend, K. Keevend, A. Gogos, A. Anthis, L. Aengenheister, S. Pratsinis, L. Plasswilm and I. Herrmann, *Chem. Mater.*, 2021, **33**, 3098.

43 L. R. H. Gerken, A. Gogos, F. H. L. Starsich, H. David, M. E. Gerdes, H. Schiefer, S. Psoroulas, D. Meer, L. Plasswilm, D. C. Weber, *et al.*, *Nat. Commun.*, 2022, **13**, 3248.

44 H. L. Nguyen, *New J. Chem.*, 2017, **41**, 14030.

45 Z. Liu, T. Wang, X. Yu, Z. Geng, Y. Sang and H. Liu, *Mater. Chem. Front.*, 2017, **1**, 1989.

46 G. Lan, K. Ni, S. S. Veroneau, X. Feng, G. T. Nash, T. Luo, Z. Xu and W. Lin, *J. Am. Chem. Soc.*, 2019, **141**, 4204.

47 Y. Chang, H. Huang, T. Yang, L. Wang, H. Zhu and C. Zhong, *J. Colloid Interface Sci.*, 2021, **599**, 785.

48 L. Wang, S. Wang, M. Li, X. Yang, F. Li, L. Xu and Y. Zou, *J. Alloys Compd.*, 2022, **909**, 164751.

49 J. Kolosnjaj-Tabi, L. Lartigue, Y. Javed, N. Luciani, T. Pellegrino, C. Wilhelm, D. Alloyeau and F. Gazeau, *Nano Today*, 2016, **11**, 280.

50 C. Wang, O. Volotskova, K. Lu, M. Ahmad, C. Sun, L. Xing and W. Lin, *J. Am. Chem. Soc.*, 2014, **136**, 6171.

51 Y. Zhao, Q. Zhang, Y. Li, R. Zhang and G. Lu, *ACS Appl. Mater. Interfaces*, 2017, **9**, 15079.

52 R. Zhou, H. Wang, Y. Yang, C. Zhang, X. Dong, J. Du, L. Yan, G. Zhang, Z. Gu and Y. Zhao, *Biomaterials*, 2019, **189**, 11.

53 Promega Corporation·2800 Woods Hollow Road·Madison, WI 53711-5399 USA, n.d.

54 A. Subiel, R. Ashmore and G. Schettino, *Theranostics*, 2016, **6**, 1651.